Journal of Electronic Materials
https://doi.org/10.1007/s11664-026-12800-6

ORIGINAL RESEARCH ARTICLE

One-Pot Fabrication of Porous $CoFe_2O_4$/Chitosan Spheres: A Bio-Magnetic Hybrid for Efficient Dye Removal

Nhan Thi Thanh Dang[1] · Nguyen Thanh Ngoc[1] · Doan Phat Huy[1] · Nguyen Hong Khanh Linh[1] · Le Loc Vuong[1]

Received: 22 December 2025 / Accepted: 5 March 2026

Abstract

Hierarchically porous $CoFe_2O_4$/chitosan ($CoFe_2O_4$/CTS) composite spheres were fabricated via a one-pot synthesis strategy, enabling controlled incorporation of magnetic cobalt ferrite nanoparticles within a biopolymer framework. Structural characterization confirmed the preservation of the spinel $CoFe_2O_4$ phase and its intimate integration within the chitosan matrix, giving rise to loading-dependent microstructural evolution. Scanning electron microscopy (SEM) and transmission electron microscopy (TEM) analyses revealed a transition from uniformly anchored nanoparticles embedded in a continuous chitosan network to partial ferrite aggregation at higher loadings, with direct implications for pore accessibility and magnetic response. Systematic variation of ferrite content established clear correlations between composite architecture, magnetic behavior, and functional performance. Adsorption experiments using representative anionic and cationic dyes served as a structure-sensitive probe, demonstrating pronounced selectivity governed primarily by the chitosan-rich matrix under neutral conditions, while ferrite loading was found to play a secondary role through its influence on porosity and magnetic recoverability. Despite partial dilution of magnetic saturation by the polymer phase, the composites retained sufficient magnetic responsiveness for efficient separation. Overall, this study provides a structure–property perspective on bio-magnetic $CoFe_2O_4$/CTS composites and highlights how controlled ferrite incorporation within a porous biopolymer scaffold can balance adsorption functionality with magnetic performance. The findings offer design guidelines for loading-tunable organic–inorganic hybrid materials relevant to separation-oriented environmental and functional applications.

Graphical Abstract

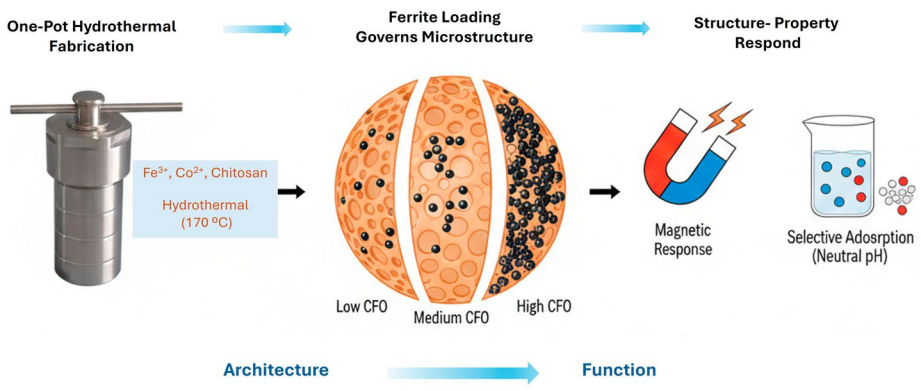

Loading-controlled microstructure and magnetic response in hierarchically porous $CoFe_2O_4$/chitosan spheres fabricated via a one-pot hydrothermal strategy.

Keywords $CoFe_2O_4$/chitosan spheres · One-pot synthesis · Bio-magnetic hybrid materials · Selective dye adsorption · Wastewater remediation

Extended author information available on the last page of the article

Published online: 17 March 2026

Introduction

The accelerated growth of the textile, pharmaceutical, and food industries has resulted in the extensive discharge of synthetic dyes into aquatic ecosystems.[1] These dyes exhibit high chemical stability and potential carcinogenicity, posing significant risks to both environmental integrity and public health.[2,3] Conventional wastewater treatment methods often fail to effectively remove such persistent organic pollutants, thereby necessitating the development of advanced adsorbent materials that align with the principles of green chemistry, including biodegradability, low secondary pollution, and ease of recovery.[4–9]

In recent years, bio-based functional composites have garnered increasing attention as sustainable alternatives to traditional inorganic adsorbents, offering promising avenues for circular and eco-efficient water purification technologies.[10–12] Among magnetic nanomaterials, cobalt ferrite ($CoFe_2O_4$) stands out due to its strong magnetization, chemical durability, and rapid magnetic separability.[13–15] However, its tendency to aggregate and limited surface functionality hinder its adsorption efficiency, particularly for structurally diverse dye molecules.[16] Chitosan (CTS), a renewable amino-polysaccharide derived from marine biomass, is widely recognized for its biocompatibility and abundance of chelation-active $–NH_2$ and –OH groups.[17,18] Nevertheless, CTS-based sorbents often suffer from poor mechanical strength and slow separation kinetics, limiting their practical applicability.[19–21]

Although previous efforts have explored the integration of $CoFe_2O_4$ with CTS, most reported strategies involve complex multistep synthesis or yield nonporous architectures, which compromise dye accessibility, magnetic recovery, and multi-pollutant removal performance.[22–28] This represents a critical gap in the design of next-generation adsorbents for emerging wastewater challenges.

In this study, we present a facile one-pot synthesis of porous $CoFe_2O_4$/chitosan ($CoFe_2O_4$/CTS) composite spheres that synergistically combine bio-derived functionality, high dye-binding affinity, and ultrafast magnetic retrievability. The resulting hybrid material exhibits superior adsorption performance toward both cationic (methylene blue—MB, crystal violet—CV) and anionic (methyl orange—MO, eosin Y—EY) dyes, surpassing conventional magnetic and biopolymeric sorbents. Furthermore, its porous architecture enhances surface accessibility and diffusion kinetics, positioning the composite as a promising candidate for scalable, zero-waste, and high-efficiency water remediation platforms.

Materials and Methods

Materials

Cobalt(II) chloride hexahydrate ($CoCl_2 \cdot 6H_2O$), ferric chloride hexahydrate ($FeCl_3 \cdot 6H_2O$), sodium hydroxide (NaOH), acetic acid (CH_3COOH), and ethylene glycol ($HOCH_2CH_2OH$) were purchased from Sigma-Aldrich (analytical grade). Chitosan (degree of deacetylation ~ 85–90%, molecular weight 200–400 kDa) was obtained from Merck and used as received. All solutions were prepared using distilled water.

Synthesis of Porous $CoFe_2O_4$/CTS Spheres

Different amounts of metal precursors were used to obtain composites with varying $CoFe_2O_4$-to-CTS ratios, while the Fe^{3+}:Co^{2+} molar ratio was adjusted to approximately 2:1 in all cases. A 20 mL mixed salt solution was first prepared by dissolving $FeCl_3$ and $CoCl_2$ in distilled water with three different molar ratios of Co^{2+}:Fe^{3+} = 0.02:0.04 (CFO/CTS-04), 0.03:0.06 (CFO/CTS-06), and 0.04:0.08 (CFO/CTS-08), followed by the addition of 1 mL CH_3COOH to assist metal–ligand coordination. Subsequently, 0.30 g of CTS was introduced into this solution and stirred at room temperature until a homogeneous [Fe^{3+},Co^{2+}]/CTS gel was obtained.

The prepared gel was transferred into a syringe and added dropwise into 200 mL of 2.0 M NaOH/ethylene glycol solution under gentle stirring. The droplets immediately polymerized into [$Co(OH)_2 \cdot Fe(OH)_3$]/CTS hydrogel spheres, which were left to stabilize for 2 h without agitation.

The collected hydrogel spheres were then subjected to hydrothermal treatment in 0.1 M NaOH at 170 °C for 8 h, during which the structure transformed into black $CoFe_2O_4$–embedded CTS spheres. Finally, the hydrothermally treated spheres were freeze-dried under vacuum at −50°C to −30°C for 24 h, yielding hierarchically porous brown–black $CoFe_2O_4$/CTS composite spheres.

Characterization

Fourier transform infrared (FT-IR) spectroscopy (Shimadzu IRPrestige-21) was employed in the range of 400–4000 cm^{-1} to examine the characteristic functional groups and metal–biopolymer coordination in CTS and the $CoFe_2O_4$/CTS composites. The crystalline structure and phase purity were analyzed using X-ray diffraction (XRD; Bruker D8 Advance X-ray diffractometer) equipped with Cu-Kα radiation (λ = 1.5418 Å, 30 kV, 10 mA) over a 2θ range of 5°–80° at a scan rate of 1° min^{-1}.

The surface morphology and microspherical architecture were observed by scanning electron microscopy (SEM; Joel JSM-6490LV), while the internal nanostructure and lattice fringes were further visualized using transmission electron microscopy (TEM; JEOL JEM-2100, 200 kV). The elemental composition of Co, Fe, C, N, and O was examined using energy-dispersive X-ray spectroscopy (EDX) attached to the SEM system. The thermal stability and organic–inorganic ratio of the composites were investigated by thermogravimetric analysis (TGA; TA Instruments Q500) under air atmosphere, with heating from 25 °C to 800 °C in steps of 10 °C min^{-1}. The magnetic properties were evaluated using a vibrating-sample magnetometer (VSM, MicroSense EZ9) at room temperature with an applied magnetic field ranging from −10 kOe to +10 kOe.

Adsorption Experiments

Materials and Stock Solutions

Analytical-grade methylene blue (MB), methyl orange (MO), eosin Y (EY), and crystal violet (CV) were used without further purification. Stock solutions (1000 mg L^{-1}) of each dye were prepared in distilled water and stored in the dark. Working solutions were prepared by serial dilution immediately prior to use.

Batch Adsorption Procedure

All adsorption experiments were conducted in batch mode using 50 mg of $CoFe_2O_4$/CTS spheres with 100 mL of aqueous dye solutions of MB, MO, EY, or CV ($C_0 = 30$ mg L^{-1}), under room temperature and magnetic stirring at 200 rpm. After the desired contact time, the $CoFe_2O_4$/CTS spheres were rapidly collected from the suspension using an external magnet. Each assay was performed in triplicate.[22,24] The residual dye concentration in the supernatant was quantified by ultraviolet–visible spectrophotometry at the corresponding maximum absorption wavelength of each dye (MB: 664 nm,[29] MO: 464 nm,[30] EY: 517 nm,[31] CV: 589 nm[32]). The adsorption performance was evaluated in terms of percentage removal (%R), equilibrium adsorption capacity (q_e), and time-dependent adsorption capacity (q_t), following standard equations in the literature.[22,24]

Percentage removal:

$$\%R = \frac{(C_0 - C_e)}{C_0} \times 100 \tag{1}$$

Amount adsorbed at time t:

$$q_t = \frac{(C_0 - C_t)V}{m} \tag{2}$$

Equilibrium adsorption capacity:

$$q_e = \frac{(C_0 - C_e)V}{m}. \tag{3}$$

Here, C_0, C_t, and C_e represent the dye concentrations (mg L^{-1}) at initial, time t, and equilibrium, respectively; V is solution volume (L), and m is the mass of the adsorbent (g).

Results and Discussion

Characterization of $CoFe_2O_4$/CTS Spheres

To elucidate the interfacial interaction between $CoFe_2O_4$ and CTS within the hybrid composite, FT-IR spectroscopy was employed (Fig. 1a). The FT-IR spectrum of pure CTS shows the characteristic vibrational features of the polysaccharide

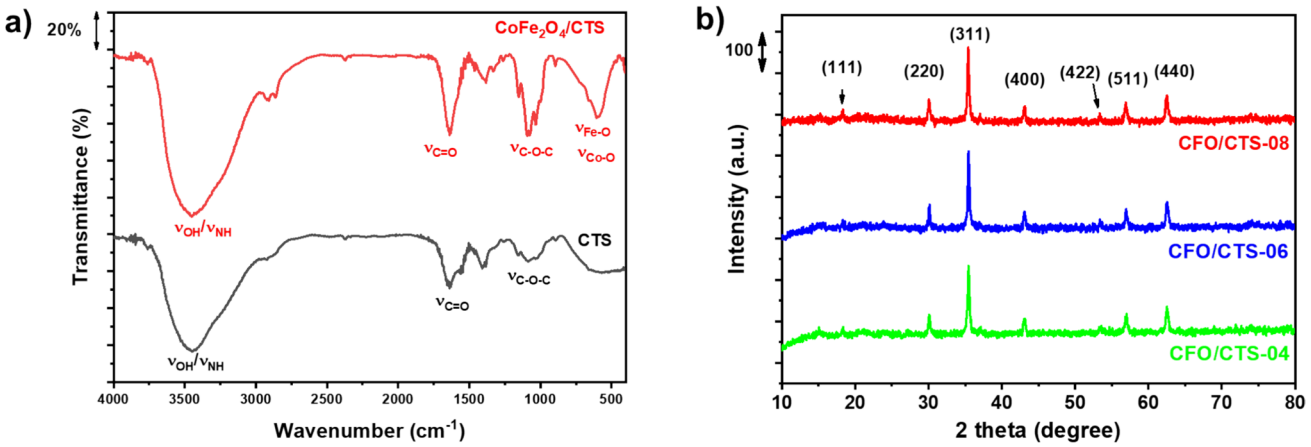

Fig. 1 Structural characterization of $CoFe_2O_4$/chitosan aerogels with varying ferrite content: (a) FT-IR spectra and (b) XRD patterns of CFO/CTS-04, CFO/CTS-06, and CFO/CTS-08.

backbone. A broad and intense band centered at 3400–3450 cm^{-1} corresponds to the overlapping O–H and N–H stretching modes, indicative of extensive intra- and intermolecular hydrogen bonding within the polymer structure. The absorption at approximately 1650 cm^{-1} is assigned to the residual amide I (C=O) stretching of partially acetylated units, while the band near 1080–1020 cm^{-1} arises from C–O–C and C–O stretching vibrations of the glucosamine rings.[33] In the $CoFe_2O_4$/CTS composite, the broad O–H/N–H stretching band is retained but slightly altered in shape and intensity, suggesting interactions between functional groups of CTS and the ferrite surface.[34] Notably, additional features appear in the 600–500 cm^{-1} region, which are characteristic of the metal–oxygen stretching modes of spinel ferrites[35]. The bands assigned to Fe–O and Co–O vibrations confirm the successful incorporation of $CoFe_2O_4$ nanoparticles into the CTS matrix.[36] Furthermore, the slight shifts and changes in intensity of the C–O–C and amide-related bands imply coordination or hydrogen-bond interactions between CTS and the metal oxide nanoparticles.[22,36] Overall, the FT-IR results demonstrate that the polymer matrix and cobalt ferrite nanoparticles interact without compromising the fundamental CTS structure, verifying the formation of a structurally integrated $CoFe_2O_4$/CTS composite.

XRD analysis was conducted to further confirm the phase formation and structural integrity of the $CoFe_2O_4$/CTS composites. Figure 1b shows the XRD patterns of the $CoFe_2O_4$/CTS composites with different ferrite loadings (CFO/CTS-04, CFO/CTS-06, and CFO/CTS-08). All samples exhibit characteristic diffraction peaks at $2\theta = 18.29°$, 30.10°, 35.43°, 43.06°, 53.45°, 56.98°, and 62.60°, respectively corresponding to the (111), (220), (311), (400), (422), (511), and (440) crystallographic planes of the cubic spinel $CoFe_2O_4$ structure, in excellent agreement with JCPDS no. 22–1086.[37,38] The complete retention of these reflections confirms the formation of a single-phase spinel ferrite with high structural purity, as no impurity-related peaks are detected.[36,39]

The diffraction peaks, in particular the intense (311) reflection, increase in intensity with higher ferrite content, indicating enhanced crystallinity and a larger proportion of $CoFe_2O_4$ in CFO/CTS-08 compared to CFO/CTS-04 and CFO/CTS-06. In contrast, broader and weaker peaks in the lower-ferrite composites suggest smaller crystallite domains and the influence of the partially amorphous CTS matrix.[22,40,41] Based on Scherrer's equation applied to the (220), (311), (400), (511), and (440) peaks, the average crystallite size of $CoFe_2O_4$ in all three composites is estimated as approximately 23–28 nm, confirming the nanoscale nature of the ferrite domains.[40,42]

The observed peak broadening across the composites, together with the moderate reduction in intensity, points to nanoscale dispersion of $CoFe_2O_4$ within the polymeric network and possible lattice strain induced at the inorganic–organic interface.[41] Importantly, hybridization with CTS does not disrupt the intrinsic crystallinity of the spinel phase; instead, it results in subtle structural modifications consistent with genuine interfacial interaction rather than simple physical blending or surface coating.

Collectively, these XRD results confirm the successful formation of structurally stable $CoFe_2O_4$/CTS hybrids and provide essential structural evidence for understanding the morphological, magnetic, and surface-property evolution discussed in the following sections.

Morphology and Microstructure

SEM and TEM analyses were performed to further elucidate the multi-scale structural characteristics of the $CoFe_2O_4$/CTS aerogel composites and to correlate their morphological evolution with increasing cobalt ferrite loading. At low magnification, all samples CFO/CTS-04 (Fig. 2a), CFO/CTS-06 (Fig. 2d), and CFO/CTS-08 (Fig. 2g) exhibit a highly porous, three-dimensional architecture typical of freeze-dried CTS aerogels, consisting of interconnected macropores with thin, smoothly interconnected pore walls. This open-cell, continuous network is advantageous for mass transport, surface accessibility, and the exposure of active sites.[43–45] Higher-magnification images reveal that the CTS pore walls possess a multilayered, wrinkled texture that remains structurally intact upon nanoparticle incorporation. In the CFO/CTS-04 sample, only a sparse population of $CoFe_2O_4$ nanoparticles is observed across the matrix; however, the nanoparticles are uniformly distributed and firmly anchored to the CTS surface (Fig. 2b and c). As the loading increases to CFO/CTS-06 (Fig. 2e and f), the pore walls become more densely decorated with $CoFe_2O_4$ nanocrystals, yet the aerogel structure remains well preserved, and the dispersion of nanoparticles remains homogeneous. At the highest loading (CFO/CTS-08, Fig. 2h and i), the surfaces appear heavily coated with densely packed ferrite nanoparticles, leading to a partial reduction in pore openness, though the hierarchical aerogel network is still identifiable.

To further verify the nanoscale dispersion and interfacial integration of $CoFe_2O_4$ nanoparticles within the CTS framework observed by SEM, TEM analysis was performed, revealing the nanoscale organization and composite formation in $CoFe_2O_4$/CTS aerogels. As shown in Fig. 3a, the CTS matrix develops into a fibrous, interconnected framework of low electron contrast, serving as a continuous scaffold for nanoparticle immobilization. Within this network, $CoFe_2O_4$ nanoparticles with cubic-like morphology are clearly distinguished (Fig. 3b–d), consistent with the spinel ferrite structure confirmed by XRD. The particles exhibit a narrow size distribution of ~10–50 nm, consistent with crystallite sizes estimated from XRD. At lower ferrite loading (CFO/

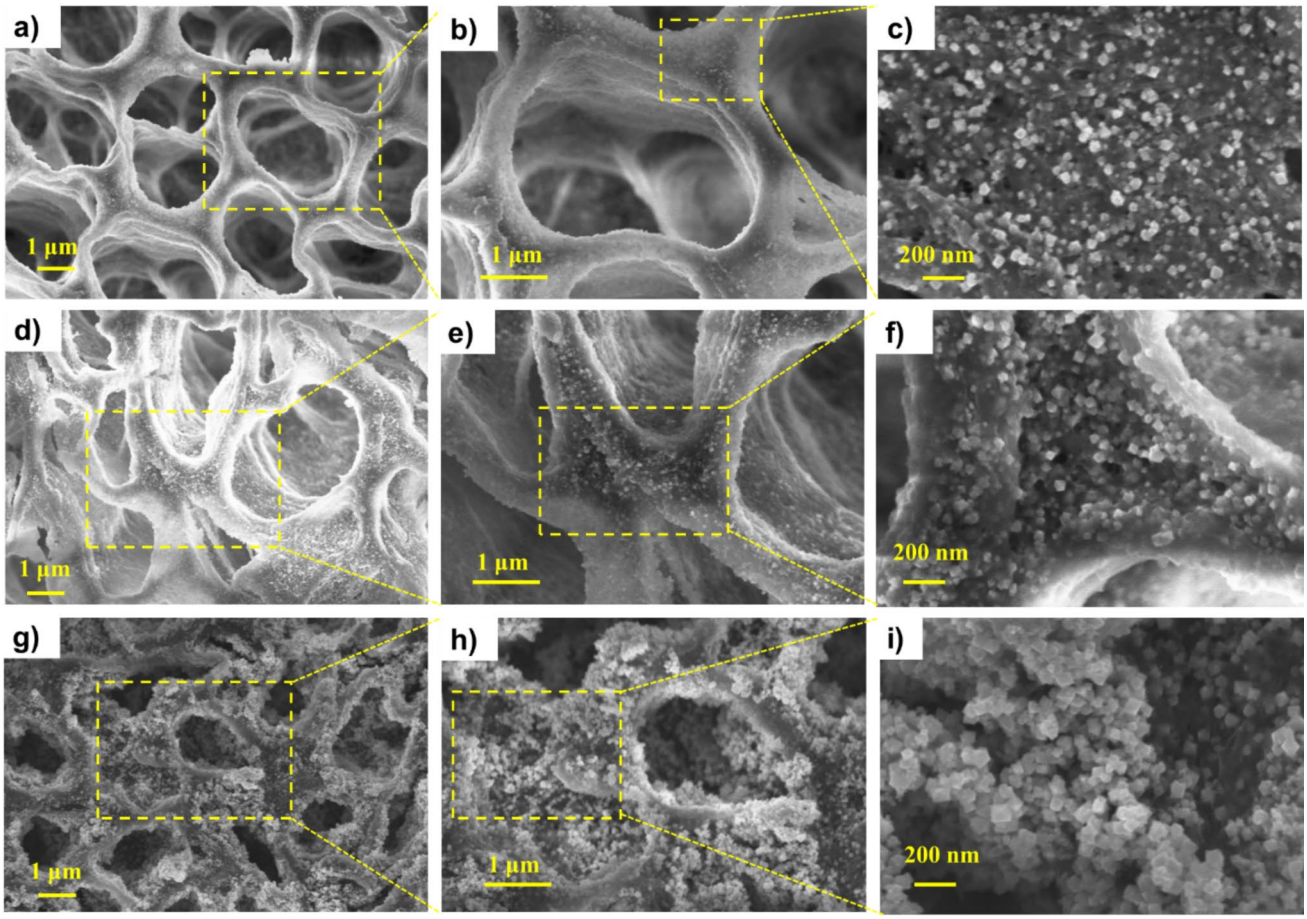

Fig. 2 SEM micrographs of CFO/CTS aerogels (a–c) CFO/CTS-04, (d–f) CFO/CTS-06, and (g–i) CFO/CTS-08, showing porous chitosan matrix and $CoFe_2O_4$ nanoparticle dispersion at low and high magnification.

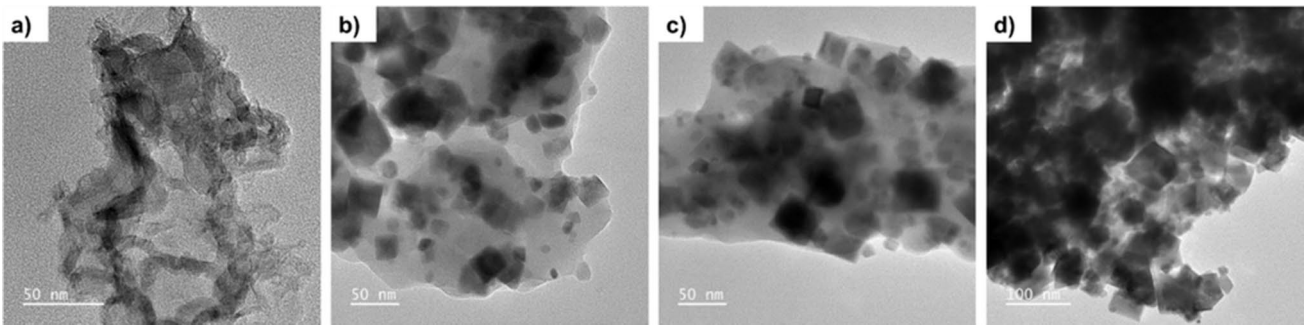

Fig. 3 TEM images of $CoFe_2O_4$/CTS composites showing (a) the aerogel-like fibrous morphology of the chitosan matrix and representative nanoparticle distribution for (b) CFO/CTS-04, (c) CFO/CTS-06, and (d) CFO/CTS-08.

CTS-04 and CFO/CTS-06), the nanoparticles are uniformly dispersed and strongly anchored along the CTS fibers, indicating that the CTS matrix effectively regulates nucleation and growth while minimizing agglomeration. This uniform dispersion reflects the interfacial interactions between $CoFe_2O_4$ and CTS functional groups ($–NH_2$, –OH), which stabilize the nanocrystals within the polymer network. At higher loading (CFO/CTS-08), denser particle populations and localized clustering appear, suggesting partial saturation of available anchoring sites. This microstructural evolution is consistent with SEM observations and underpins the loading-dependent changes in magnetic properties and pore accessibility discussed later. Overall, TEM confirms the successful construction of a hierarchically organized

organic–inorganic composite, with $CoFe_2O_4$ nanoparticles intimately integrated into the CTS matrix. This architecture preserves the magnetic functionality of cobalt ferrite while ensuring structural stability and accessibility of active sites.[46–48]

To complement the SEM and TEM analyses, EDX characterization was employed to confirm the elemental composition and to examine changes associated with different ferrite loadings of the $CoFe_2O_4$/CTS composites. Representative EDX spectra of CFO/CTS-04, CFO/CTS-06, and CFO/CTS-08 are presented in Fig. 4. All spectra exhibit strong signals corresponding to C, N, and O, which originate from the CTS matrix, along with characteristic Fe and Co peaks associated with the $CoFe_2O_4$ nanoparticles, confirming the coexistence of organic and inorganic components within the composites. The relative intensity of the Fe K and Co K peaks systematically increases from sample CFO/CTS-04 to sample CFO/CTS-08, consistent with the intentional increase in $CoFe_2O_4$ content. In sample CFO/CTS-04 (Fig. 4a), Fe and Co account for 13.66 wt% and 6.08 wt%, respectively; these values increase to 15.81 wt% Fe and 8.18 wt% Co in sample CFO/CTS-06 (Fig. 4b), and reach 24.35 wt% Fe and 10.77 wt% Co in sample CFO/CTS-08 (Fig. 4c). This monotonic increase in metal content confirms the effective incorporation and controlled adjustment of the ferrite fraction within the composite.[26,36]

The Fe-to-Co ratios obtained from the EDX spectra are consistent with the expected stoichiometry of the spinel $CoFe_2O_4$ phase, with Fe present at approximately twice the concentration of Co. Meanwhile, the gradual decrease in the relative carbon and nitrogen content reflects the reduced proportion of CTS as the ferrite loading increases. No additional peaks attributable to extraneous elements are detected, indicating that the synthesis yields chemically clean composites without detectable secondary phases. Overall, the EDX results provide compositional support for the structural and magnetic analyses, demonstrating that ferrite loading can be systematically tuned while preserving the chemical integrity of both the $CoFe_2O_4$ and CTS components.[34,49]

Thermal Stability

The thermal behavior of pure CTS and the $CoFe_2O_4$/CTS composites was evaluated using TGA–derivative thermogravimetry (DTG), as shown in Fig. 5a. The CTS sample exhibits a two-stage degradation profile typical of polysaccharide-based biopolymers. The initial weight loss below 150 °C corresponds to the removal of physically adsorbed and bound water. The major decomposition event occurs between approximately 250 °C and 350 °C, where a sharp DTG peak is observed, reflecting the depolymerization and thermal cleavage of chitosan's glycosidic linkages and the breakdown of its acetylated and amine-bearing units. Beyond 400 °C, CTS undergoes continuous mass loss associated with carbonization, leaving a relatively small residual mass at 800–900°C.[17,50,51]

In contrast, all $CoFe_2O_4$/CTS composites exhibit markedly enhanced thermal stability compared to pure CTS. The composites show a similar initial dehydration stage, but the onset of the main degradation step is shifted to higher temperatures, and the corresponding DTG peaks become broader and less intense, indicating a more gradual decomposition. This stabilization effect is attributed to interactions between the polymer matrix and the $CoFe_2O_4$ nanoparticles, which restrict the heat-induced mobility of the CTS chains.[25,36,52] Furthermore, the total weight loss of the composites is significantly reduced; the residual mass increases systematically with higher ferrite content (CFO/CTS-04 < CFO/CTS-06 < CFO/CTS-08), consistent with the presence of a thermally robust metal oxide. Based on the residual mass remaining at approximately 850–900°C after complete decomposition of the organic matrix, the $CoFe_2O_4$ content in CFO/CTS-04, CFO/CTS-06, and CFO/CTS-08 was estimated at 31.6 wt%, 42.5 wt%, and 49.2 wt%, respectively. These values confirm the effective and controlled incorporation of cobalt ferrite within the CTS matrix. The higher char yield and attenuated DTG intensity confirm that incorporation of $CoFe_2O_4$ serves as an effective thermal reinforcement.[53,54] Overall, the TGA–DTG results

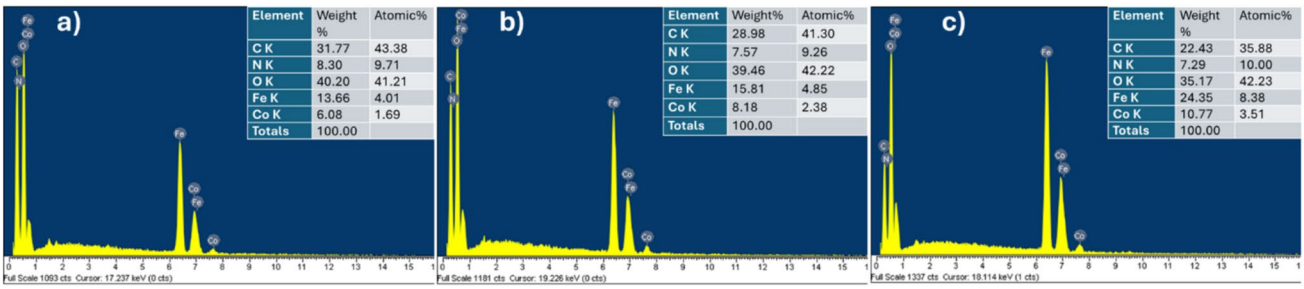

Fig. 4 EDX spectra of $CoFe_2O_4$/chitosan aerogels with different ferrite loadings: (a) CFO/CTS-04, (b) CFO/CTS-06, and (c) CFO/CTS-08. The spectra were collected from representative regions of the SEM images shown in Fig. 2, confirming the presence and loading-dependent increase in Co and Fe elements within the chitosan matrix.

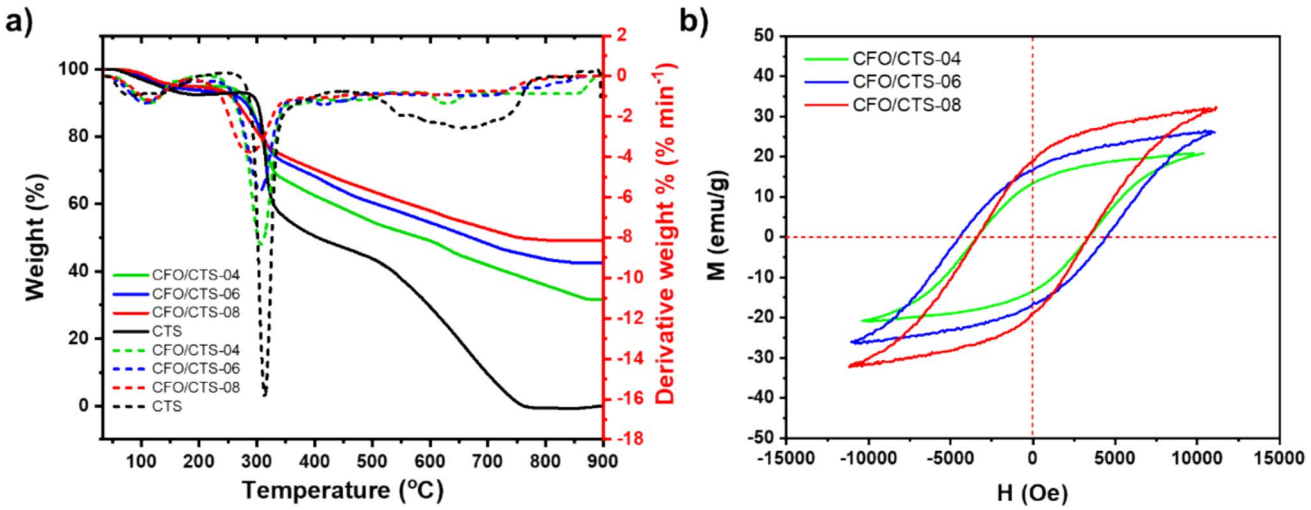

Fig. 5 Thermal and magnetic properties of $CoFe_2O_4$/chitosan aerogels with different ferrite loadings: (a) TGA–DTA thermograms and (b) room-temperature VSM magnetization curves of CFO/CTS-04, CFO/CTS-06, and CFO/CTS-08.

demonstrate that embedding $CoFe_2O_4$ nanoparticles substantially improves the thermal resistance of CTS, and the extent of this enhancement correlates positively with the ferrite content of the composites.

Magnetic Properties

To evaluate the magnetic behavior of the $CoFe_2O_4$/CTS composites and elucidate the influence of ferrite loading, room-temperature VSM measurements were performed, and the corresponding hysteresis loops are shown in Fig. 5b. All samples exhibit clear ferromagnetic behavior, characterized by well-defined hysteresis loops that confirm the preservation of the ferrimagnetic spinel $CoFe_2O_4$ phase after incorporation into the CTS framework.[55,56] A pronounced increase in saturation magnetization (M_s) is observed with increasing ferrite content: 20.83 emu g^{-1} for CFO/CTS-04, 26.13 emu g^{-1} for CFO/CTS-06, and 32.26 emu g^{-1} for CFO/CTS-08. This trend reflects the progressively higher fraction of magnetic nanoparticles within the composite and is consistent with previous reports on $CoFe_2O_4$–biopolymer systems, where M_s scales with ferrite loading due to the dominant contribution of the inorganic magnetic phase.[40,57]

Coercivity (Hc) and remanent magnetization (M_r) also vary across the samples. Specifically, CFO/CTS-04, CFO/CTS-06, and CFO/CTS-08 exhibit Hc values of 3390 Oe, 4465 Oe, and 3390 Oe, respectively, while their M_r values are 13.46 emu g^{-1}, 16.87 emu g^{-1}, and 18.94 emu g^{-1}. The higher coercivity observed in CFO/CTS-06 suggests stronger dipole interactions and reduced interparticle spacing at intermediate ferrite loading, whereas the comparable Hc values of CFO/CTS-04 and CFO/CTS-08 indicate that excessive ferrite incorporation may promote partial aggregation, thereby diminishing coercivity.[56,57] In contrast, the monotonic increase in M_r with ferrite content confirms the increasing contribution of the magnetic phase to the overall remanent response. The moderately wide hysteresis loops correspond to single-domain or pseudo–single-domain magnetic behavior, characteristic of nanoscale cobalt ferrite particles with crystallite sizes around 20–30 nm. The absence of superparamagnetic behavior at room temperature aligns with literature findings for $CoFe_2O_4$ nanocrystals above the superparamagnetic threshold (~10–15 nm), indicating that thermal fluctuations are insufficient to randomize the magnetic moments in these composites.[55–57]

Overall, the VSM results demonstrate that the magnetic properties of $CoFe_2O_4$/CTS aerogel composites can be effectively tuned by adjusting ferrite content, with M_s and M_r scaling with nanoparticle loading, while Hc exhibits a nonlinear dependence due to particle distribution and aggregation effects. This tunability provides flexibility for optimizing the composites for magnetic separation, environmental remediation, targeted delivery, and catalytic applications, where strong and stable magnetic responsiveness is highly advantageous.[40,56]

Adsorption Performance of $CoFe_2O_4$/CTS Composites Toward Organic Dyes

Although $CoFe_2O_4$/CTS composites have been studied as magnetic adsorbents, most previously reported materials possess low porosity and have been evaluated against only a limited range of dyes.[22–25,27,41] As a result, the adsorption behavior of highly porous $CoFe_2O_4$/CTS structures and their performance toward both anionic and cationic dyes remain insufficiently explored.[22,24,25,27,49] In this work, a $CoFe_2O_4$/

CTS aerogel with a porous architecture is synthesized, and its adsorption capability is systematically assessed using four representative dyes—eosin Y (EY), methyl orange (MO), methylene blue (MB), and crystal violet (CV)—to probe structure-related performance trends.

At neutral pH, the $CoFe_2O_4$/CTS aerogel exhibits markedly distinct adsorption behavior toward structurally diverse dyes, underscoring a mechanistic selectivity that has been overlooked in prior studies. The adsorption profiles of the CFO/CTS-04 sample (Fig. 6a and b) reveal a pronounced preference for anionic species: EY and MO achieve high maximum adsorption capacity of 62.2 mg g^{-1} and 58.7 mg g^{-1}, respectively, and are removed with exceptionally high efficiency of 99.1% and 96.7%. Both dyes reach equilibrium rapidly within 20–40 min, which can be attributed to the interconnected porous network facilitating mass transport, together with favorable interaction between the CTS-rich matrix and negatively charged dye species under near-neutral conditions.[22,28,58] In contrast, cationic dyes MB and CV display much lower capacity of 25.8 mg g^{-1} and 17.9 mg g^{-1}, with removal efficiency of only 42.2% and 29.6%, and require longer time (60–120 min) to stabilize. This diminished uptake is consistent with a less favorable interaction environment at pH 7, where the composite surface—dominated by protonated amino groups of CTS and ferrite-associated hydroxyls—provides limited negative charge density for effective binding of cationic species.[49,59,60] These observations suggest that surface charge characteristics in combination with pore accessibility play an important role in governing adsorption trends rather than a single dominant mechanism.[61,62]

The effect of ferrite loading on adsorption behavior was further examined by comparing CFO/CTS-04, CFO/CTS-06, and CFO/CTS-08 aerogels (Fig. 6). Only modest variations in adsorption performance are observed across the three samples. For anionic dyes, EY and MO consistently exhibit high removal efficiency (98.8–99.2% for EY and 95.9–97.7% for MO) and comparable maximum adsorption capacity (61.9–62.2 mg g^{-1} for EY and 58.2–59.3 mg g^{-1} for MO) across all samples. These results suggest that adsorption is predominantly governed by the CTS-rich, positively charged aerogel matrix, where the porous architecture and abundant protonated amino groups provide strong electrostatic attraction toward anionic dye molecules. Increasing the ferrite fraction beyond a certain level therefore provides limited additional enhancement to dye uptake, as the primary adsorption sites remain associated with the polymer matrix.[17,62,63] In contrast, cationic dyes MB and CV consistently display low removal efficiency (42.2–44.2% for MB and 28.9–31.8% for CV) and limited adsorption capacity (25.8–27.0 mg g^{-1} for MB and 17.5–19.3 mg g^{-1} for CV), regardless of ferrite loading. The slight variations observed among the composites may be attributed to minor changes in surface area or pore accessibility, or nanoparticle dispersion induced by higher ferrite incorporation.[22,64] Moreover, higher ferrite incorporation may reduce the proportion of

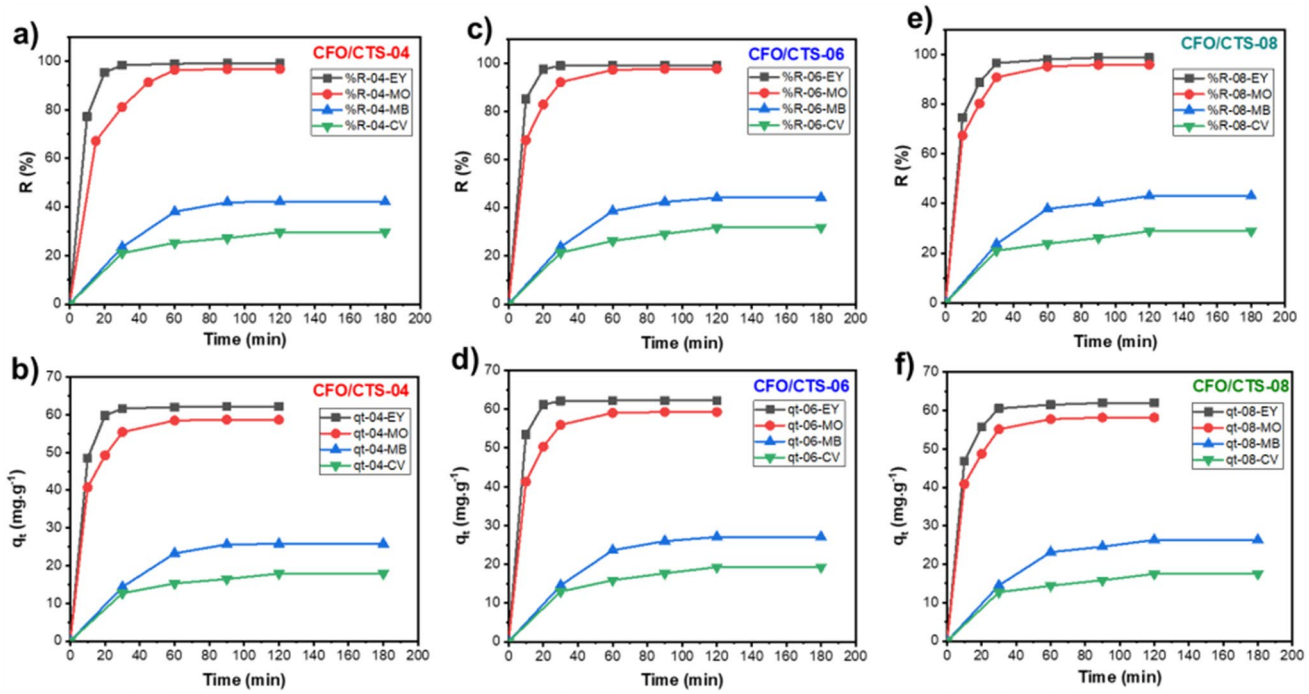

Fig. 6 Time-dependent adsorption capacity (q_t) and removal efficiency (R%) of CFO/CTS aerogels: (a, b) CFO/CTS-04, (c, d) CFO/CTS-06, and (e, f) CFO/CTS-08, evaluated for four dyes (eosin Y, methyl orange, methylene blue, and crystal violet) at pH 7.

accessible amino groups and partially block pores, further constraining adsorption of cationic species.[58,65,66]

Taken together, these results indicate that the adsorption performance of $CoFe_2O_4$/CTS aerogels is governed primarily by the interplay between surface charge characteristics, porous architecture, and nanoparticle distribution within the composite, while variations in ferrite loading exert a secondary influence. Adsorption is therefore treated here as a structure-dependent functional response rather than as evidence for a single, definitive adsorption mechanism. This comparative analysis of anionic and cationic dyes within a highly porous $CoFe_2O_4$/CTS framework provides insight into how composite architecture influences adsorption behavior in bio-magnetic hybrid materials.

Although chitosan–ferrite hybrid materials prepared via one-pot strategies have been reported previously, the present work provides a distinct structure–property perspective by systematically elucidating how ferrite loading governs the hierarchical architecture and functional performance of porous $CoFe_2O_4$/CTS spheres. Rather than focusing solely on adsorption capacity, this study demonstrates that variations in $CoFe_2O_4$ content induce a clear microstructural evolution, from uniformly anchored nanoparticles within a continuous CTS network to partial clustering at higher loadings. This transition directly influences pore accessibility, magnetic response, and recoverability, highlighting the critical role of nanoparticle dispersion and interfacial integration in determining composite functionality. The combined SEM, TEM, and EDX analyses establish a direct correlation between nanoscale organization and macroscopic magnetic behavior, offering insight into how inorganic loading modulates the balance between structural integrity and magnetic efficiency. Such a loading-dependent structure–property relationship has not been explicitly addressed in prior chitosan–ferrite adsorption studies and provides a materials-design guideline for optimizing bio-magnetic composites beyond empirical performance metrics.

Conclusion

In this work, hierarchically porous $CoFe_2O_4$/chitosan composite spheres were successfully fabricated via a one-pot synthesis strategy, enabling controlled incorporation of magnetic ferrite nanoparticles within a biopolymer framework. Beyond demonstrating adsorption capability, this study elucidates how systematic variation of ferrite loading governs the multi-scale structure and functional response of the composites. Structural and morphological analyses reveal a clear loading-dependent microstructural evolution, ranging from uniformly anchored $CoFe_2O_4$ nanoparticles within a continuous CTS network to partial nanoparticle clustering at higher ferrite content.

This structural transition is shown to influence pore accessibility, thermal stability, and magnetic behavior, highlighting the importance of nanoparticle dispersion and interfacial integration in determining composite performance. The correlation established between nanoscale organization and macroscopic magnetic response provides a structure–property perspective that extends beyond empirical adsorption metrics commonly reported for chitosan–ferrite systems. Adsorption studies using representative anionic and cationic dyes further illustrate how these loading-dependent structural features translate into selective functional responses governed primarily by the CTS-rich matrix under neutral conditions.

Overall, the insights gained from this work contribute to a deeper understanding of loading-controlled architecture–property relationships in organic–inorganic hybrid materials. The one-pot strategy presented here offers a practical materials-design approach for balancing porosity, magnetic functionality, and structural integrity, and provides design guidelines for optimizing porous magnetic composites for separation-oriented environmental and other functional applications.

Acknowledgments This work was supported by the University of Education, Hue University [Grant Number NCTBSV.T24-TN.104-02].

Conflict of interest The authors declare that they have no conflict of interest.

References

1. V. Katheresan, J. Kansedo, and S.Y. Lau, Efficiency of various recent wastewater dye removal methods: a review. *J. Environ. Chem. Eng.* 6, 4676 (2018).
2. V.K. Gupta, and Suhas, Application of low-cost adsorbents for dye removal—a review. *J. Environ. Manag.* 90, 2313 (2009).
3. E. Forgacs, T. Cserháti, and G. Oros, Removal of synthetic dyes from wastewaters: a review. *Environ. Int.* 30, 953 (2004).
4. C.I. Pearce, J.R. Lloyd, and J.T. Guthrie, The removal of colour from textile wastewater using whole bacterial cells: a review. *Dyes Pigm.* 58, 179 (2003).
5. G. Crini, Non-conventional low-cost adsorbents for dye removal: A review. *Bioresour. Technol.* 97, 1061 (2006).
6. C.R. Holkar, A.J. Jadhav, D.V. Pinjari, N.M. Mahamuni, and A.B. Pandit, A critical review on textile wastewater treatments: possible approaches. *J. Environ. Manag.* 182, 351 (2016).
7. Y. Liu, B. Biswas, M. Hassan, and R. Naidu, Green adsorbents for environmental remediation: synthesis methods, ecotoxicity, and reusability prospects. *Processes* 12, 1195 (2024).
8. K. Mohanrasu, A.C. Manivannan, H.J.R. Rengarajan, R. Kandaiah, A. Ravindran, L. Panneerselvan, T. Palanisami, and C.I. Sathish, Eco-friendly biopolymers and composites: a sustainable development of adsorbents for the removal of pollutants from wastewater. *Mater. Sustain.* 3, 13 (2025).
9. H. Alkhaldi, S. Alharthi, S. Alharthi, H.A. AlGhamdi, Y.M. AlZahrani, S.A. Mahmoud, L.G. Amin, N.H. Al-Shaalan, W.E. Boraie, M.S. Attia, N. Aldaleeli, M.M. Ghobashy, S.A. Al-Gahtany, A.I. Sharshir, M. Madani, R. Darweshk, and S.F.

Abaza, Sustainable polymeric adsorbents for adsorption-based water remediation and pathogen deactivation: a review. *RSC Adv.* 14, 33143–33190 (2024).
10. J.J. Andrew, and H.N. Dhakal, Sustainable biobased composites for advanced applications: recent trends and future opportunities—a critical review. *Compos. Part C: Open Access* 7, 100220 (2022).
11. W. Al-Gethami, M.A. Qamar, M. Shariq, A.N.M.A. Alaghaz, A. Farhan, A.A. Areshi, and M.H. Alnasir, Emerging environmentally friendly bio-based nanocomposites for the efficient removal of dyes and micropollutants from wastewater by adsorption: a comprehensive review. *RSC Adv.* 14, 2804 (2024).
12. M. Faheem, and K.A. Khan, Harnessing sustainable biocomposites: a review of advances in greener materials and manufacturing strategies. *Polym. Bull.* 82, 8827 (2025).
13. P.A. Vinosha, A. Manikandan, A.C. Preetha, A. Dinesh, Y. Slimani, M.A. Almessiere, A. Baykal, B. Xavier, and G.F. Nirmala, Review on recent advances of synthesis, magnetic properties, and water treatment applications of cobalt ferrite nanoparticles and nanocomposites. *J. Supercond. Nov. Magn.* 34, 995 (2021).
14. S.M. Ansari, A. Younis, Y.D. Kolekar, and C.V. Ramana, Cobalt ferrite nanoparticles: the physics, synthesis, properties, and applications. *Appl. Phys. Rev.* 12, 21308 (2025).
15. A. Mudhoo, and M. Sillanpää, Magnetic nanoadsorbents for micropollutant removal in real water treatment: a review. *Environ. Chem. Lett.* 19, 4393 (2021).
16. Y. Krishnan, K. Babu, S. Sakkaraiyan, A. Dinesh, A. Shanmugam, K. Radhakrishnan, and M. Ayyar, Spinel cobalt ferrite nanoparticles for photocatalysts, sensor and biomedical applications: a review. *Semiconductors* 58, 721 (2024).
17. M. Rinaudo, Chitin and chitosan: properties and applications. *Prog. Polym. Sci.* 31, 603 (2006).
18. S.L. Zou, X.R. Liu, J.H. Zhang, Y.C. Xu, Q. Wang, L.P. Xiao, and R.C. Sun, Advanced functionalization strategies of chitin and chitosan toward sustainable nanocomposites. *Carbohydr. Polym.* 373, 124648 (2026).
19. G.V. de Brião, J.R. de Andrade, M.G.C. da Silva, and M.G.A. Vieira, Removal of toxic metals from water using chitosan-based magnetic adsorbents: a review. *Environ. Chem. Lett.* 18, 1145 (2020).
20. A. Spoială, C.I. Ilie, D. Ficai, A. Ficai, and E. Andronescu, Chitosan-based nanocomposite polymeric membranes for water purification—a review. *Materials* 14, 2091 (2021).
21. X. Zang, R. Jiang, H.Y. Zhu, Q. Wang, Y.Q. Fu, D.X. Zhao, J.B. Li, and H. Liu, A review on the progress of magnetic chitosan-based materials in water purification and solid-phase extraction of contaminants. *Sep. Purif. Technol.* 330, 125521 (2024).
22. C.M. Simonescu, A. Tătăruş, D.C. Culiţă, N. Stănică, I.A. Ionescu, B. Butoi, and A.-M. Banici, Comparative study of $CoFe_2O_4$ nanoparticles and $CoFe_2O_4$-chitosan composite for congo red and methyl orange removal by adsorption. *Nanomaterials* 11, 1 (2021).
23. Y. Zhang, T. Yan, L. Yan, X. Guo, L. Cui, Q. Wei, and B. Du, Preparation of novel cobalt ferrite/chitosan grafted with graphene composite as effective adsorbents for mercury ions. *J. Mol. Liq.* 198, 381 (2014).
24. J.M.N. dos Santos, C.R. Pereira, L.A.A. Pinto, T. Frantz, É.C. Lima, E.L. Foletto, and G.L. Dotto, Synthesis of a novel $CoFe_2O_4$/chitosan magnetic composite for fast adsorption of indigotine blue dye. *Carbohydr. Polym.* 217, 6 (2019).
25. S.P. Sahare, A.V. Wankhade, A.K. Sinha, and S.P. Zodape, Modified cobalt ferrite entrapped chitosan beads as a magnetic adsorbent for effective removal of malachite green and copper (II) Ions from aqueous solutions. *J. Inorg. Organomet. Polym. Mater.* 33, 266 (2023).
26. D. Gingasu, I. Mindru, L. Patron, A. Ianculescu, E. Vasile, G. Marinescu, S. Preda, L. Diamandescu, O. Oprea, M. Popa, C. Saviuc, and M.C. Chifiriuc, Synthesis and characterization of chitosan-coated cobalt ferrite nanoparticles and their antimicrobial activity. *J. Inorg. Organomet. Polym. Mater.* 28, 1932 (2018).
27. N. Tabassum, R. Anjum, P. Haque, Md.S. Hossain, M.B. Mobarak, Md.S. Quddus, F. Chowdhury, L. Rahman, D. Islam, S. Ahmed, and M. Mahmud, Ag-Co ferrite-based magnetic polymeric composite film: a breakthrough in cationic dye remediation for sustainable environment. *RSC Adv.* 14, 36557 (2024).
28. N.M. Hosseini, S. Sheshmani, and A.S. Shahvelayati, Manganese ferrite-graphite oxide-chitosan nanocomposite for efficient dye removal from aqueous and textile wastewater under UV and sunlight irradiation. *Sci. Rep.* 15, 866 (2025).
29. I. Khan, K. Saeed, I. Zekker, B. Zhang, A.H. Hendi, A. Ahmad, S. Ahmad, N. Zada, H. Ahmad, L.A. Shah, T. Shah, and I. Khan, Review on methylene blue: its properties, uses, toxicity and photodegradation. *Water (Switzerland)* 14, 242 (2022).
30. F.C. Tsai, N. Ma, T.C. Chiang, L.C. Tsai, J.J. Shi, Y. Xia, T. Jiang, S.-K. Su, and F.-S. Chuang, Adsorptive removal of methyl orange from aqueous solution with crosslinking chitosan microspheres. *J. Water Process Eng.* 1, 2 (2014).
31. A. Hossain, A.B.M.S. Rayhan, Md.J. Raihan, A. Nargis, I.M.I. Ismail, A. Habib, and A.J. Mahmood, Kinetics of degradation of Eosin Y by one of the advanced oxidation processes (AOPs)—Fenton's process. *Am. J. Anal. Chem.* 07, 863 (2016).
32. Y.P. Huang, H.B. Niu, L. Jin, L. Jiao, D. Johnson, H.L. Tian, S. Sarina, H.-Y. Zhu, and Y.-F. Fang, Selective adsorption of crystal violet via hydrogen bonded water bridges by $InVO_4$. *Chem. Eng. J. Adv.* 15, 100508 (2023).
33. J. Brugnerotto, J. Lizardi, F.M. Goycoolea, W.A. Èelles-Monal, J.D. Áres, and M. Rinaudo, An infrared investigation in relation with chitin and chitosan characterization. *Polymer (Guildf)* 42, 3569 (2001).
34. I. Anila, and M.J. Mathew, Study on the physico-chemical properties, magnetic phase resolution and cytotoxicity behavior of chitosan-coated cobalt ferrite nanocubes. *Appl. Surf. Sci.* 556, 149791 (2021).
35. D.F. Katowah, M.M. Rahman, M.A. Hussein, T.R. Sobahi, M.A. Gabal, M.M. Alam, and A.M. Asiri, Ternary nanocomposite based poly(pyrrole-co-O-toluidine), cobalt ferrite and decorated chitosan as a selective Co^{2+} cationic sensor. *Compos. B Eng.* 175, 107175 (2019).
36. S. Briceño, J. Suarez, and G. Gonzalez, Solvothermal synthesis of cobalt ferrite hollow spheres with chitosan. *Mater. Sci. Eng. C* 78, 842 (2017).
37. V.P. Senthil, J. Gajendiran, S.G. Raj, T. Shanmugavel, G.R. Kumar, and C.P. Reddy, Study of structural and magnetic properties of cobalt ferrite ($CoFe_2O_4$) nanostructures. *Chem. Phys. Lett.* 695, 19 (2018).
38. T.A.S. Ferreira, J.C. Waerenborgh, M.H.R.M. Mendonça, M.R. Nunes, and F.M. Costa, Structural and morphological characterization of $FeCo_2O_4$ and $CoFe_2O_4$ spinels prepared by a coprecipitation method. *Solid State Sci.* 5, 383 (2003).
39. Z. Zi, Y. Sun, X. Zhu, Z. Yang, J. Dai, and W. Song, Synthesis and magnetic properties of $CoFe_2O_4$ ferrite nanoparticles. *J. Magn. Magn. Mater.* 321, 1251 (2009).
40. M.M. Arman, and S.I. El-Dek, Structural, surface, magnetic study and application of nanoparticles $CoFe_2O_4$, ZnO and its nanocomposite. *J. Supercond. Nov. Magn.* 36, 1913 (2023).
41. M. Malakootian, A. Nasiri, and H. Mahdizadeh, Preparation of $CoFe_2O_4$/activated carbon@chitosan as a new magnetic nanobiocomposite for adsorption of ciprofloxacin in aqueous solutions. *Water Sci. Technol.* 78, 2158 (2018).
42. A.A. El-Fadl, A.M. Hassan, and M.A. Kassem, Tunable cationic distribution and structure-related magnetic and optical properties

by Cr^{3+} substitution for Zn^{2+} in nanocrystalline Ni-Zn ferrites. *Results Phys.* 28, 104622 (2021).
43. R. Balzarotti, M. Ambrosetti, M. Arnesano, A. Anglani, G. Groppi, and E. Tronconi, Periodic open cellular structures (POCS) as enhanced catalyst supports: optimization of the coating procedure and analysis of mass transport. *Appl. Catal. B* 283, 119651 (2021).
44. J. Wu, F. Xu, S. Li, P. Ma, X. Zhang, Q. Liu, R. Fu, and D. Wu, Porous polymers as multifunctional material platforms toward task-specific applications. *Adv. Mater.* 31, 1802922 (2018).
45. M.H. Sun, S.Z. Huang, L.H. Chen, Y. Li, X.Y. Yang, Z.Y. Yuan, and B.-L. Su, Applications of hierarchically structured porous materials from energy storage and conversion, catalysis, photocatalysis, adsorption, separation, and sensing to biomedicine. *Chem. Soc. Rev.* 45, 3479 (2016).
46. B. Boury, and S. Plumejeau, Metal oxides and polysaccharides: an efficient hybrid association for materials chemistry. *Green Chem.* 17, 72 (2015).
47. S. Kalia, S. Kango, A. Kumar, Y. Haldorai, B. Kumari, and R. Kumar, Magnetic polymer nanocomposites for environmental and biomedical applications. *Colloid Polym. Sci.* 292, 2025 (2014).
48. I.B. Amor, H. Hemmami, N. Grara, O. Aidat, A.B. Amor, S. Zeghoud, and S. Bellucci, Chitosan: a green approach to metallic nanoparticle/nanocomposite synthesis and applications. *Polym Basel* 16, 2662 (2024).
49. S. Ahmad, S.A. Shah, and S. Ahmed, A new chitosan Schiff base-modified cobalt ferrite: mechanistic insights and performance enhancement in photocatalysis of Rhodamine B dye and antibacterial applications. *Int. J. Biol. Macromol.* 283, 136841 (2024).
50. C.G.T. Neto, J.A. Giacometti, A.E. Job, F.C. Ferreira, J.L.C. Fonseca, and M.R. Pereira, Thermal analysis of chitosan based networks. *Carbohydr. Polym.* 62, 97 (2005).
51. H. Moussout, H. Ahlafi, M. Aazza, and M. Bourakhouadar, Kinetics and mechanism of the thermal degradation of biopolymers chitin and chitosan using thermogravimetric analysis. *Polym. Degrad. Stab.* 130, 1 (2016).
52. A.A. Kajani, A. Pouresmaeili, and M. Kamali, Facile one-pot synthesis of the mesoporous chitosan-coated cobalt ferrite nanozyme as an antibacterial and MRI contrast agent. *RSC Adv.* 14, 16801 (2024).
53. J.B. Marroquin, K.Y. Rhee, and S.J. Park, Chitosan nanocomposite films: Enhanced electrical conductivity, thermal stability, and mechanical properties. *Carbohydr. Polym.* 92, 1783 (2013).
54. H.M. Dardeer, A.S. Ibrahim, A.N. Gad, and A.A.M. Gaber, Bifunctional of Fe_3O_4@chitosan nanocomposite as a clarifying agent and cationic flocculant on different sugar solutions as a comprehensive semi industrial application. *Sci. Rep.* 14, 1848 (2024).
55. D.H. Manh, T.D. Thanh, T.L. Phan, and D.S. Yang, Towards hard-magnetic behavior of $CoFe_2O_4$ nanoparticles: a detailed study of crystalline and electronic structures, and magnetic properties. *RSC Adv.* 13, 8163 (2023).
56. N.J. Mdlalose, W.B. Mdlalose, S.T. Dlamini, and S.R. Mokhosi, Investigating the structural and magnetic properties of chitosan coated $CoFe_2O_4$ nanoparticles for drug delivery. *Arch. Biomed. Eng. Biotechnol.* 3, 1 (2020).
57. Y. Kumar, and P.M. Shirage, Highest coercivity and considerable saturation magnetization of $CoFe_2O_4$ nanoparticles with tunable band gap prepared by thermal decomposition approach. *J. Mater. Sci.* 52, 4840 (2017).
58. T.M. Freire, L.M.U.D. Fechine, D.C. Queiroz, R.M. Freire, J.C. Denardin, N.M.P.S. Ricardo, T.N.B. Rodrigues, D.R. Gondim, I.J.S. Junior, and P.B.A. Fechine, Magnetic porous controlled Fe_3O_4-chitosan nanostructure: an ecofriendly adsorbent for efficient removal of AZO dyes. *Nanomaterials* 10, 1194 (2020).
59. D.W. Cho, B.H. Jeon, C.M. Chon, F.W. Schwartz, Y. Jeong, and H. Song, Magnetic chitosan composite for adsorption of cationic and anionic dyes in aqueous solution. *J. Ind. Eng. Chem.* 28, 60 (2015).
60. X. Liu, X. Zhao, Y. Liu, and T. Zhang, Review on preparation and adsorption properties of chitosan and chitosan composites. *Polym. Bull.* 79, 2633 (2022).
61. M. Bellaj, K. Aziz, M. El Achaby, M. El Haddad, L. Gebrati, T.A. Kurniawan, Z. Chen, P.-S. Yap, and F. Aziz, Cationic and anionic dyes adsorption from wastewater by clay-chitosan composite: an integrated experimental and modeling study. *Chem. Eng. Sci.* 285, 119615 (2024).
62. W.S. Wan Ngah, L.C. Teong, and M.A.K.M. Hanafiah, Adsorption of dyes and heavy metal ions by chitosan composites: a review. *Carbohydr. Polym.* 83, 1446 (2011).
63. A. Mokhtar, S. Abdelkrim, A. Djelad, A. Sardi, B. Boukoussa, M. Sassi, and A. Bengueddach, Adsorption behavior of cationic and anionic dyes on magadiite-chitosan composite beads. *Carbohydr. Polym.* 229, 115399 (2020).
64. M.A. Abdelaziz, M.E. Owda, R.E. Abouzeid, O. Alaysuy, and I. Mohamed, Kinetics, isotherms, and mechanism of removing cationic and anionic dyes from aqueous solutions using chitosan/magnetite/silver nanoparticles. *Int. J. Biol. Macromol.* 225, 1462 (2023).
65. M.A. Ahmed, M.F.A. Messih, S.F. El-Hafez, and A.M.M. Khalifa, Synthesis of metallic silver nanoparticles decorated mesoporous SnO_2 for removal of methylene blue dye by coupling adsorption and photocatalytic processes. *J. Photochem. Photobiol. A Chem.* 346, 77 (2017).
66. D.C. da Silva Alves, B. Healy, LAd.A. Pinto, T.R.S. Cadaval, and C.B. Breslin, Recent developments in Chitosan-based adsorbents for the removal of pollutants from aqueous environments. *Molecules* 26, 594 (2021).

Authors and Affiliations

Nhan Thi Thanh Dang[1] · Nguyen Thanh Ngoc[1] · Doan Phat Huy[1] · Nguyen Hong Khanh Linh[1] · Le Loc Vuong[1]

✉ Nhan Thi Thanh Dang
nhandang@hueuni.edu.vn;
dangthithanhnhan@dhsphue.edu.vn

Nguyen Thanh Ngoc
ntngoc@dhsphue.edu.vn

Doan Phat Huy
doanphathuy.090804@gmail.com

Nguyen Hong Khanh Linh
linhnguyen250905@gmail.com

Le Loc Vuong
lelocvuong3@gmail.com

[1] Faculty of Chemistry, University of Education, Hue University, 34 Le Loi, Hue 530000, Vietnam